JOURNAL OF MATERIALS SCIENCE 31 (1996) 4817–4829

Thermo-mechanical fatigue degradation of a nickel-aluminide coating on a single-crystal nickel-based alloy

P. MORETTO, J. BRESSERS
Institute for Advanced Materials, Joint Research Centre, CEC, P.O.B.2, 1755 ZG, Petten, The Netherlands

A microstructural study of the degradation of an NiAl coating on a nickel-base single crystal subjected to thermo-mechanical (TMF) and low-cycle fatigue (LCF) has been made, using scanning electron microscopy and energy and wavelength dispersive spectrometry. Various thermal histories were investigated, and the associated coating degradation mechanisms identified. Under TMF conditions the hot part of the cycle (950–1050 °C) helps to stabilize the β-phase of the coating. Surface oxidation proceeds slowly and does not affect the bulk of the coating. Evidence of enhanced outward aluminium diffusion and inward oxygen diffusion was found at long exposure times. Fatigue cracks initiate at the surface, grow intergranularly through the coating and are frequently arrested at the coating–substrate interface. In LCF conditions, massive oxidation of the surface and interdiffusion at the coating–substrate interface cause NiAl decomposition into first γ′ and later γ phases. Cracks initiate and grow through the coating in a mode similar to the TMF case.

1. Introduction

Single-crystal nickel-base alloys are frequently used as blade materials in aero gas turbines because of their excellent resistance to high-temperature deformation. Owing to the trend to higher chromium contents, the sensitivity of the alloys towards high-temperature oxidation increases. Coatings are therefore applied in order to provide the blades with adequate protection against environmental degradation and loss of mechanical performance. Aluminide coatings, formed by diffusing aluminium into the nickel-base alloy in the so-called pack aluminization process, are commonly used on gas turbine blades. A number of studies, investigating the nature and the extent of the influence of the presence of a coating on the mechanical performance of nickel-base superalloys, report either detrimental or beneficial/neutral effects on specific, isothermally measured mechanical properties of the substrate [1–7]. When subjected to thermo-mechanical fatigue (TMF) cycling, the presence of a coating is reported as detrimental [8] or beneficial [9, 10] to the TMF life. As the result of the adverse effect of the presence of the coating on the mechanical behaviour of the blade material, attention towards the characterization and the degradation mechanisms of the coating has recently increased. In particular, Shen *et al.* [11, 12] and King and co-workers [13, 14] recently reported the complex metallurgical phenomena taking place in NiAl coatings during heat treatment and ageing, and Holmes and McClintock [15] also reported results from cyclic thermal fatigue tests.

The major cause of failure in current single-crystal blades of aero gas turbines is thermally induced stresses, which result from thermal strains over the blade thickness caused by temperature gradients during heating and cooling cycles. Isothermal fatigue data, which are traditionally used for blade design purposes, do not account for the damage and failure processes occurring in blades exposed to thermal fatigue cycles. In particular, the effect of the phase shift between the temperature and strain cycles occurring in some parts of the blade cannot be reproduced in isothermal fatigue tests. Moreover blades provided with aluminide coatings are expected to display a non-isothermal fatigue behaviour because of the ductile–brittle transition of the coating at approximately 750 °C. Actual blade behaviour is more closely simulated by thermo-mechanical fatigue tests, which are designed to reproduce the temperature and strain cycles seen by critical volume elements of the blade. As opposed to isothermal fatigue testing, during TMF cycling the coated test specimen is repeatedly cycled through the ductile–brittle transition temperature of the coating, which is expected to result in different damage and failure mechanisms.

As part of a wider study on the TMF behaviour of single-crystal nickel-base alloys in the uncoated and coated conditions, the effect of TMF and LCF cycling on the microstructure of a NiAl-coated single-crystal nickel-based alloy has been investigated, and the results are reported here. The main degradation mechanisms are identified and compared to the effects of ageing and high-temperature exposure reported in the literature.

0022–2461

TABLE I Nominal and measured RR2000 average bulk composition and measured γ and γ′ composition (concentrations in at %)

	Al	Ti	V	Cr	Co	Mo	Ni
Nominal composition	11.1	4.6	1.1	10.9	13.9	1.7	57.8
Average (WDS)	11.7	4.6	1.4	10.6	13.8	1.8	56.2
Average (EDS)	12.5	4.6	1.1	10.3	13.3	2.3	56.0

2. Experimental procedure

2.1. Material

The substrate was RR2000, a high γ′ volume content single-crystal nickel-base alloy of gas turbine quality with alloying additions (wt %) of 15% Co, 10% Cr, 5.5% Al, 4% Ti, 3% Mo, 1% V and 0.015% C (see Table I for atomic concentrations). The crystallographic orientation of the long axis of all the test specimens was within 12° of ⟨0 0 1⟩. Single-crystal blanks of the substrate were solution treated for 4 h at 1260 °C, gas fan quenched to 800 °C and air-cooled to room temperature. The blanks were machined into TMF and low-cycle fatigue (LCF) specimens and subsequently high-activity pack aluminized for 4 h at 870 °C, followed by a 1 h diffusion treatment at 1100 °C and an ageing treatment for 16 h at 850 °C in an argon atmosphere. The pack aluminization treatment resulted in isotropic polycrystalline coatings of typically 40 μm thickness. The microstructure of the substrate consists of a γ phase and γ′ precipitates with a cuboidal shape, ranging in edge length from 0.2–0.8 μm, peaking at 0.4 μm. In addition, $M_{23}C_6$ carbides are common throughout the matrix.

2.2. TMF testing

The TMF test specimen has end parts with a cylindrical geometry, separated by a solid guage length with a rectangular cross-section of 12 mm × 3 mm. The edges of the gauge length section are rounded in order to promote good adherence of the coating. The specimen machining procedure is optimized so as to inhibit recrystallization of the worked zone during heat treatment. The surface finish in the gauge length of the substrate material is $R_a = 0.05$ μm. The coated specimens are tested in the as-received condition, without further surface modification treatment.

A major variable in TMF testing is the phase relationship between the temperature and the mechanical strain cycle. One of the most damaging cycle types is the − 135 °C lag, $R = 0$ cycle, in which the temperature lags 135 °C with respect to the mechanical strain. This TMF cycle was included in a study aimed at investigating the effect of the presence of the coating on the TMF life, the results of which are reported elsewhere [16]. The minimum and maximum cycle temperatures were 300 and 1050 °C, respectively. R is the ratio between the minimum and maximum strains in the cycle. Linear heating and cooling rates of 25 and 12.5 °C s^{-1}, respectively, were applied, resulting in a cycle period of 90 s. The mechanical strain rates were approximately 2×10^{-4} and 1×10^{-4} s^{-1} during heating and cooling, respectively.

In addition to the TMF tests, coated specimens were low-cycle fatigue tested at 1050 °C, applying similar loading and unloading rates as in the TMF tests. Samples with specific TMF and LCF testing conditions but with different times to rupture were selected for detailed microstructural investigation of the coating. The corresponding testing conditions and the results are listed in Table II.

2.3. Analytical techniques

For qualitative and quantitative microchemical analysis, an EPMA equipment with three wavelength dispersive spectrometers was used (CAMECA sx50). Typical acquisition conditions were 15 kV, 10 s per element and beam currents between 5 and 80 nA. For all the metals, pure standards were used, while for carbon, a silicon carbide material was chosen. The quantification was performed by means of PAP software [17]. No correction was applied for the peak overlapping between VK_α and TiK_β. This causes an error in the concentration of vanadium of typically 0.3–0.4 wt % which is considered negligible. A comparison between the nominal composition of the SRR99 and the EPMA result can be seen in Table I. In this case, the electron beam was defocused in order to determine an average bulk composition.

More serious problems are encountered with respect to quantifying carbon, notably sample surface contamination and overlap with the second-order line of CrK_α. Both effects contribute to overestimating the carbon content. The two sources of error contribute to overestimating of the carbon content by approximately 2–3 wt %, making the identification of low carbon content carbides, such as M_6C, nearly impossible. The overlapping problem was tackled by acquiring the peaks in an integral mode and by subtracting the CrK_α^2 signal using a commercial fitting software as shown in Fig. 1 in the case of $Cr_{23}C_6$. However,

TABLE II TMF and LCF testing conditions and results

Spec.	Cycle type C	T (°C)	Δε (%)	σ_{min} (MPa)	σ_{max} (MPa)	N_f cycles	Time spent above 950 °C (h)
TMF-A	− 135 °C lag $R = 0$	300–1050	0.75	− 291	658	1930	6.4
TMF-B	− 135 °C lag $R = 0$	300 –1050	0.55	− 11	571	27500	91.0
LCF-A	$R = 0$	1040	1.20	− 174	200	1305	32.6
LCF-B	$R = 0$	1050	0.55	− 125	129	4422	110.6

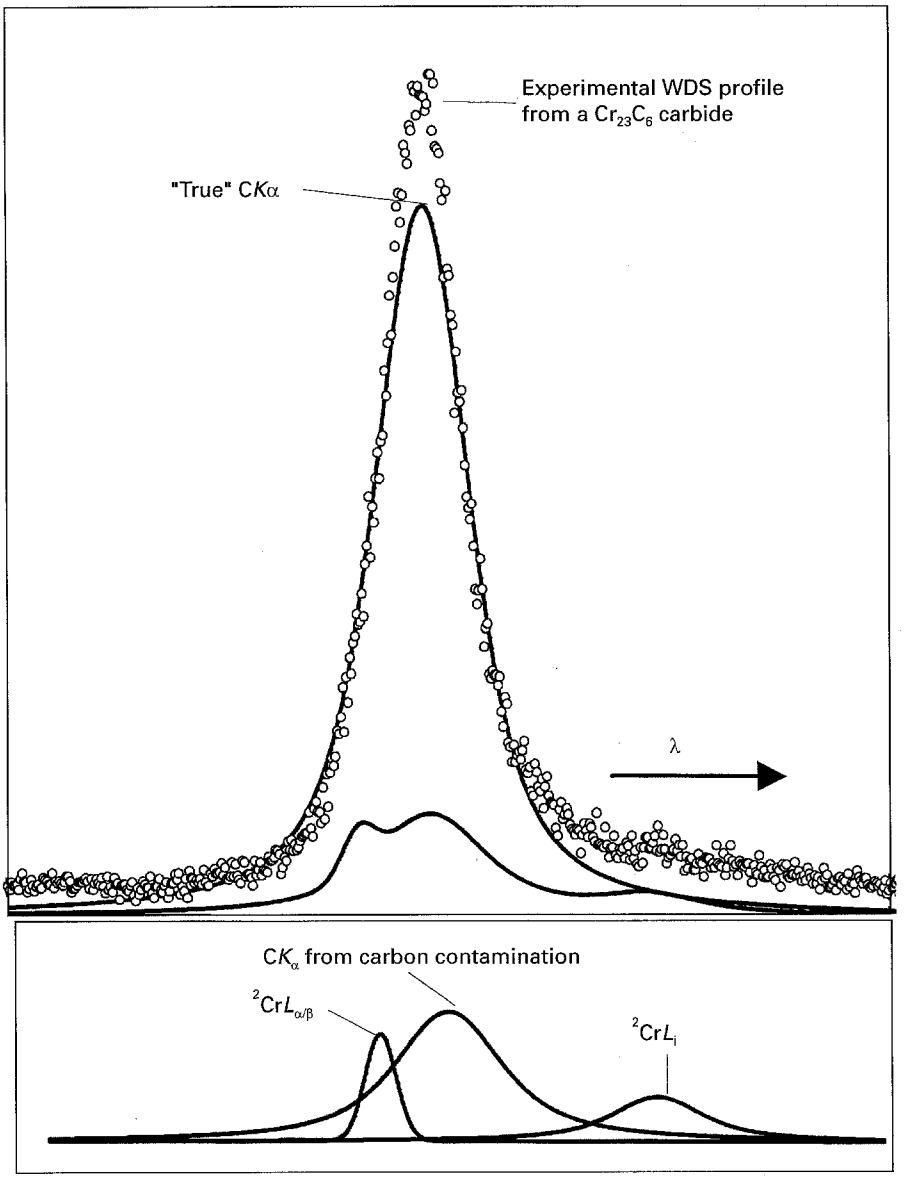

Figure 1 Experimental WDS profile around the 4.48 nm X-ray wavelength from a $Cr_{23}C_6$ carbide and its deconvolution into the CK_α, the CrL_α^2 and the carbon contamination contributions.

the surface contamination is assumed to be equal in the case of the chromium and SiC standards and in the unknown sample, an assumption which is not always verifiable in practice. This deconvolution is anyway impossible in the analysis of low carbon contents (for example, the M_6C and $M_{18}C$ carbides), because the surface contamination contribution to the carbon signal totally shadows the material contribution.

The spatial resolution of the microprobe ranges between 1 and 2 μm, and is determined not only by the spread of the electrons inside the solid matter, but also by the rather high beam diameter due to the relatively high currents used. In cases of precipitates of the order of 1 μm and smaller, an energy dispersive spectrometer (Sigma, KEVEX), mounted on an SEM microscope (DSM 940, Zeiss), was used. Because of the lower current used in this instrument, the spatial resolution can be pushed to 1 μm or lower. The EDS spectra were processed by standardless analysis and the quantification obtained by PAP-based software. The accuracy of the results was inferior compared to the analysis with standards by WDS, with an absolute uncertainty in the worst cases as high as $\pm$ 0.5 wt %. Still, the results of the two techniques were found to be consistent. In presenting the results, WDS analyses are preferred in all the cases without particular resolution requirements.

3. Results

In the following sections, the various samples are characterized in detail from the morphological and analytical point of view. Fig. 2 shows a sketched overview of the principal microstructural features characteristic of the different testing conditions. The numbers refer to the WDS or EDS point analyses of Tables III–V.

3.1. As-received material

Fig. 3a and b shows the material in its starting condition, in a cross-section perpendicular to the ⟨0 0 1⟩ direction, while Fig. 4 presents a WDS quantitative

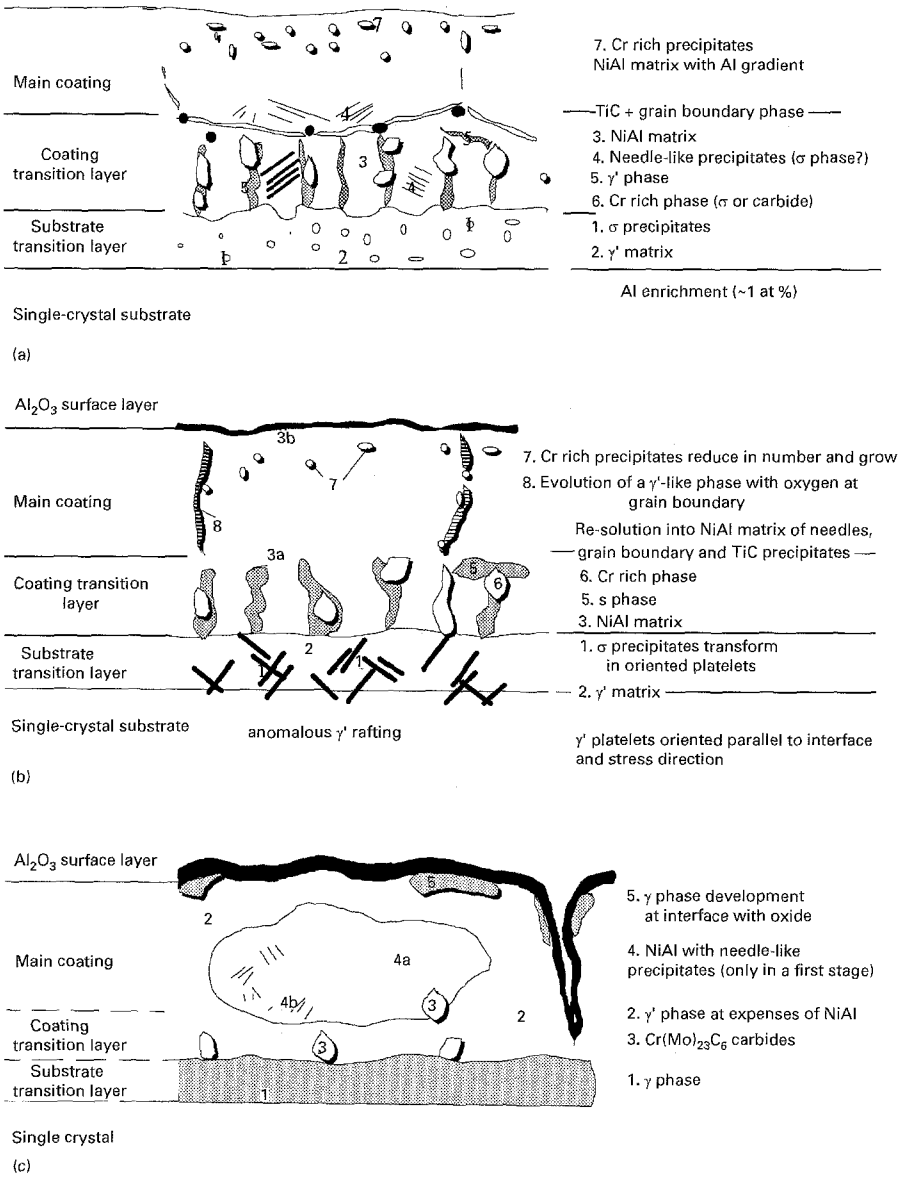

Figure 2 Overview of the main microstructural features for the (a) as-received, (b) TMF-tested and (c) LCF-tested samples.

TABLE III Analysis results of the various phases of as-received sample (the numbers refer to the position given in Fig. 2a)

Phase		Concentrations (at %)							
		Al	Ti	V	Cr	Co	Mo	Ni	
Average composition in bulk single crystal									
15 μm below transition layer		11.4	4.5	1.0	9.6	12.7	2.1	58.7	EDS
5 μm below transition layer		12.5	4.6	1.1	9.9	12.9	2.3	56.8	EDS
Coating transition layer									
β-NiAl-Matrix	3	34.2	4.3	1.0	3.9	10.6	0.2	45.8	WDS
Needle-like precipitates[a]	4	29.3	4.8	0.8	5.9	10.9	0.3	48.1	EDS
Phase 1 at grain boundary[a]	5	17.4	8.2	1.1	2.3	10.2	0.9	60.1	EDS
Phase 2 at grain boundary[a]	6	2.3	1.2	2.3	40.4	19.1	17.9	16.9	EDS
Main coating									
Just above coating transition layer		35.0	3.6	0.9	6.2	9.8	0.4	44.2	WDS
At surface		42.9	0.8	0.4	4.0	8.3	0.4	41.1	WDS

[a] Typical dimension lower than 1 μm, concentrations analysis contains contributions of surrounding phase(s).

line scan from the bulk up to the external surface. Following the terminology of Gale and King [13], a substrate transition layer, a coating transition layer and a main coating layer can be distinguished. Point analyses of the various phases are given in Table III.

The substrate transition layer shows round, 0.1–0.5 μm large precipitates rich in chromium and

TABLE IV Analysis results of the various phases of the TMF-B sample (the numbers refer to the position given in Fig. 2b)

Phase		Concentrations (at %)							
		Al	Ti	V	Cr	Co	Mo	Ni	
Average composition in bulk single crystal									
Bulk – dendrite	–	9.2	3.9	1.5	12.9	15.5	2.0	55.1	WDS
Bulk – interdendrite	–	10.7	4.4	1.4	11.5	14.5	1.9	55.6	WDS
Bulk – just below substrate transition layer	–	13.0	4.6	1.6	11.7	14.6	1.9	52.6	WDS
Substrate transition layer									
Matrix	2	14.1	7.7	1.2	3.6	11.5	0.3	61.6	EDS
Needles[a]	1	–	1.0	1.7	42.7	23.2	12.3	19.2	EDS
Coating transition layer									
Phase 1 at grain boundary[a]	5	–	1.2	2.9	44.9	26.0	6.2	19.2	EDS
Phase 2 at grain boundary[a]	6	–	0.4	4.0	78.5	3.5	8.2	5.4	EDS
Main coating									
TMF-A β-NiAl matrix just above coating transition layer	3a	32.1	3.1	0.6	4.6	10.1	0.8	48.9	EDS
TMF-A β-NiAl matrix at surface	3b	34.8	1.6	0.2	4.2	9.2	1.1	48.8	EDS
TMF-B β-NiAl matrix just above coating transition layer	3a	32.3	3.7	0.8	4.6	11.1	0.3	47.2	WDS
TMF-B β-NiAl matrix at surface	3b	34.3	2.5	0.7	4.4	9.5	0.4	48.2	WDS
Round precipitates	7	–	0.4	1.5	41.2	22.6	18.3	16.1	EDS
Grain-boundary phase	8	16.1	7.2	1.0	3.0	11.9	0.5	60.8	EDS

[a] Typical dimension smaller than 1 μm, analysis contains contributions of surrounding phases(s).

TABLE V Analysis results of the various phases of the LCF-B sample (the numbers refer to the position given in Fig. 2c)

Phase		Concentrations (at %)							
		Al	Ti	V	Cr	Co	Mo	Ni	
Average composition in bulk single crystal									
γ matrix	–	7.0	1.5	0.8	18.0	19.0	2.4	51.1	WDS
γ′ platelet	–	14.8	4.5	0.7	4.1	9.9	0.7	65.4	WDS
Coating transition layer									
Substrate transition layer	1	9.2	1.7	1.5	20.0	20.1	3.5	44.1	WDS
γ′ layer	2	16.7	4.5	1.0	4.4	11.7	1.0	60.6	WDS
Particles	3	Carb. 20.3	0.2	2.1	63.2	2.5	7.7	4.1	WDS
Main coating									
β-NiAl islands	4	31.3	1.7	0.6	5.4	9.9	0.4	50.7	WDS
Needle-like precipitates in β-NiAl (only LCF-A)	4 B	24.3	2.7	0.7	7.2	11.3	0.4	53.4	EDS
Phase in contact with oxide	5	10.0	1.3	1.2	18.9	19.8	2.9	45.9	WDS

molybdenum (not resolved in the maps), finely dispersed in a continuous matrix, yet too small to enable analysis by means of the available techniques. The matrix can be identified with the γ′ phase on the basis of BSE contrast observations and literature results. Below this zone the single-crystal substrate presents an enrichment of 1% in aluminium with respect to its bulk concentration.

The coating transition layer consists of an understoichiometric NiAl matrix (β phase) and of types of precipitations aligned perpendicular to the interface: one, light grey by BSE imaging (point 5), presents a composition comparable with the γ′-phase in the bulk, but with a considerably higher titanium content, while the second precipitation type shows chromium contents up to 40% and can be tentatively identified as a σ phase of composition $(Cr_{0.8}Mo_{0.2})_3(NiCo)_2$ (see, for example, [18], where a general formula for that phase is given). Inside the NiAl grains, needle-like precipitates can be seen. Although their analysis results are contaminated by the surrounding matrix (point 4), they show a trend to lower aluminium and higher chromium and titanium contents, while molybdenum and cobalt remain unchanged. These needles can be reasonably interpreted as γ′-precipitates. The needles extend further across the main coating–coating transition layer interface. The interface is characterized by a line of TiC precipitates (black by BSE imaging in Fig. 3a) and by a, presumably γ′, grain-boundary phase.

In the main coating layer, a precipitate-free zone can be seen, followed by a zone up to the surface

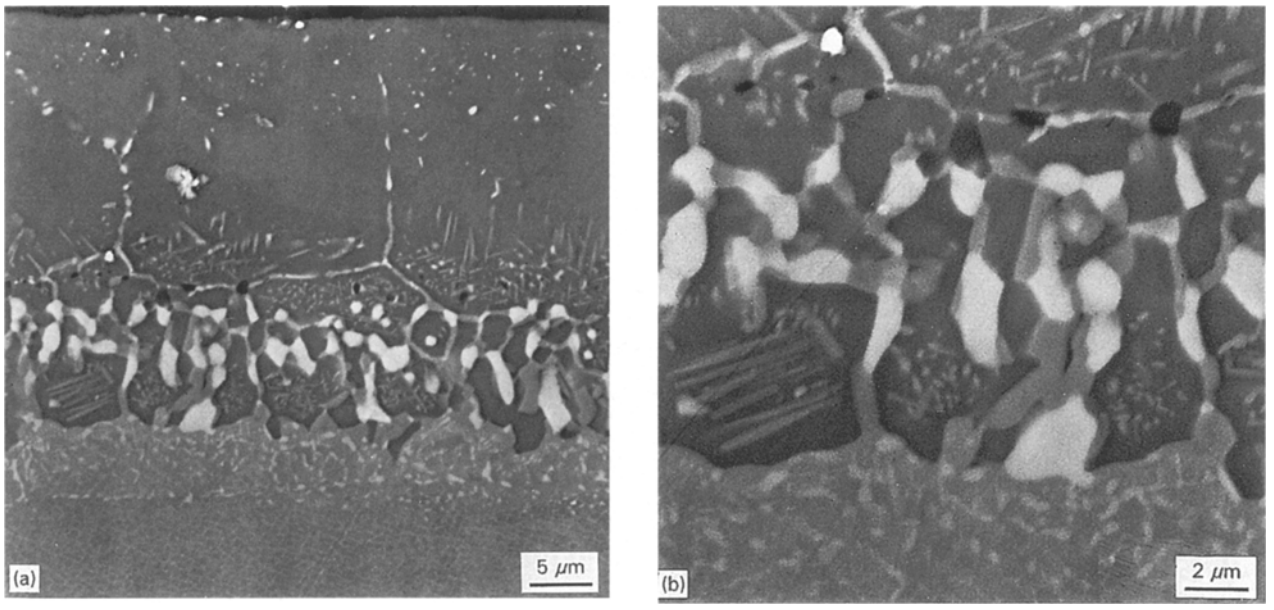

Figure 3 (a, b) BSE images of the cross-section of the as-received sample: coating surface is at the top, single crystal at the bottom.

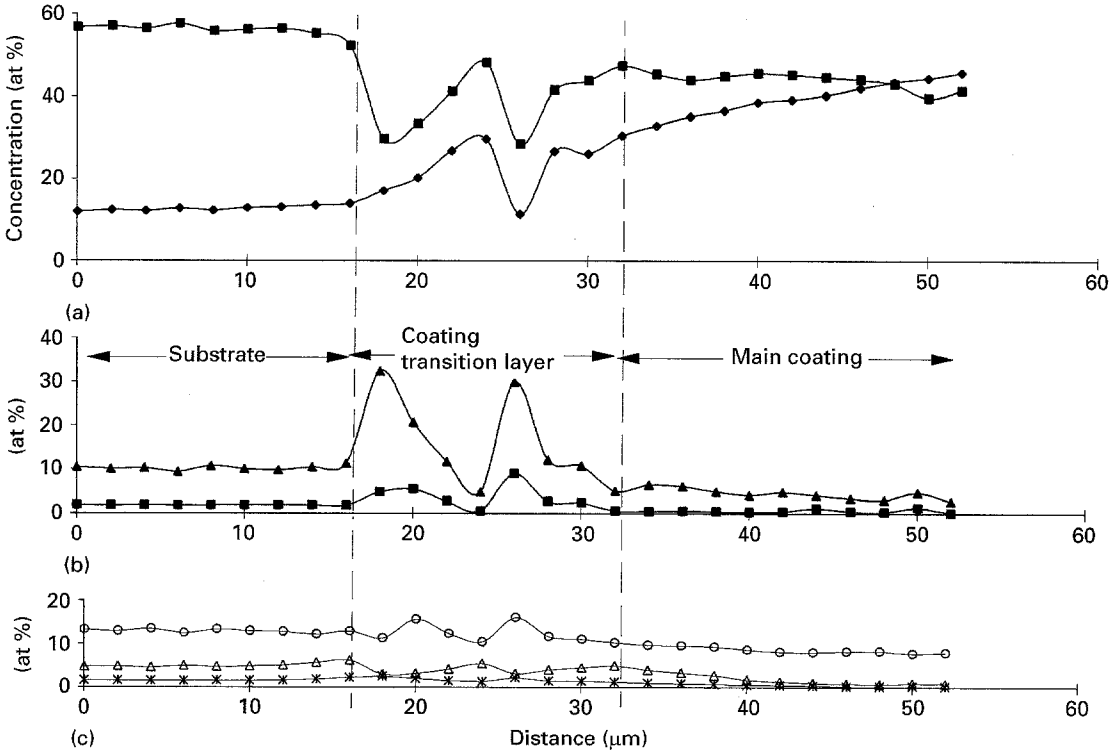

Figure 4 WDS line scans perpendicular to the coating of the as-received sample. (a) (◆) Al, (■) Ni; (b) (■) Mo, (▲) Cr; (c) (*) V, (△) Ti, (○) Co.

with small round precipitates, rich in chromium and molybdenum. The main coating-consists on NiAl with a strong aluminium gradient: as the line profile in Fig. 4 and the analyses in Table III show, the aluminium to nickel atomic ratio varies from 0.7 at the interface with the coating transition layer up to 1.0 at the surface. In contrast, the aluminium content in the NiAl matrix of the transition layer is approximately constant. No carbides of the form $M_{23}C_6$ were found. If present, their dimension is below the limit of detectability (tens of nanometres).

3.2. TMF tested samples

The high-temperature exposure and the development of an aluminium oxide layer during TMF tests causes a redistribution of elements and evident changes in the morphology of the nickel aluminide coating. Fig. 5a and b shows typical cross-sections of, respectively, samples TMF-A and TMF-B, in a plane parallel to the stress axis. The testing conditions of the two samples are identical from the thermal point of view. Because only the number of cycles to rupture varies radically, their microstructure is characteristic of the

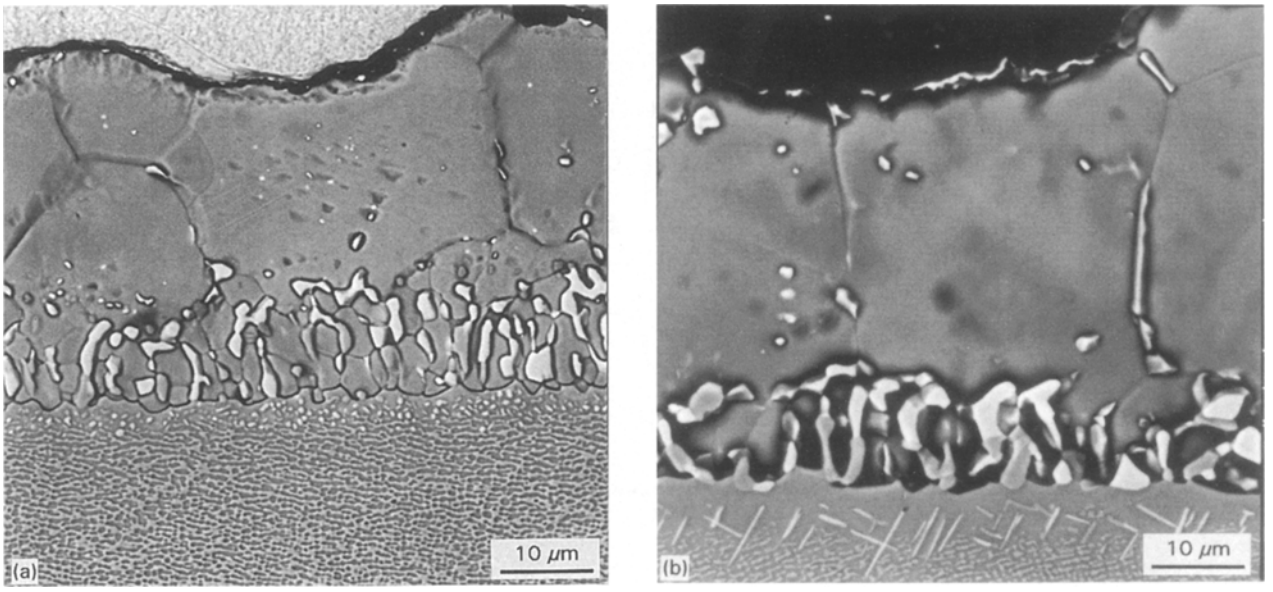

Figure 5 (a, b) BSE images of the cross-section of thermo-mechanical fatigued sample: (a) TMF-A, (b) TMF-B. Coating surface is at the top, single crystal at the bottom.

coating degradation at two different fatigue times. Conventionally, assuming 950 °C as the lower temperature limit for rapid diffusional processes, the exposure times to diffusion of samples TMF-A and TMF-B are 6.4 and 91 h, respectively.

The coating surface is covered by an approximately 1.0–2.0 μm thick Al_2O_3 layer, containing finely dispersed titanium oxide particles. The surface appears very rough in comparison with the as-received case, with top-to-valley variations of typically 10 μm. Neither the oxide scale thickness nor the surface roughness evolve considerably with increasing TMF exposure. In most of the cases, cracks in the coating begin at the external surface, develop perpendicular to it in an intergranular way, and are arrested at or just below the coating–substrate transition layers interface. Occasionally, cracks branch off in the coating transition zone. The cracks are filled with Al_2O_3, and covered at their internal surfaces by a continuous γ' layer in TMF-B, while only occasionally γ' islands are found inside the cracks of the TMF-A sample. At the crack tips, mixed nickel and chromium oxides form. Cracks of another type are also observed in the TMF-B sample, apparently restricted to the coating transition layer and the main coating (Fig. 6), without any connection with the surface. Also, inside these cracks an oxide scale and γ' layers are present, with characteristics identical to those of the "external" cracks.

Table IV contains point analyses and Fig. 7 shows the concentration profiles for the TMF-B sample. The formation of Al_2O_3 at the surface causes the aluminium gradient across the main coating to flatten out already in the first hours (compare β-NiAl matrix analyses for TMF-A and B in Table IV). The main coating consists of NiAl strongly understoichiometric in aluminium (Al to Ni ratio of 0.71). Also the needle-like precipitates in the main coating and in the coating transition layers dissolve into the NiAl matrix early in the TMF life. The originally finger-like precipitates in the coating transition layer tend to grow and round-

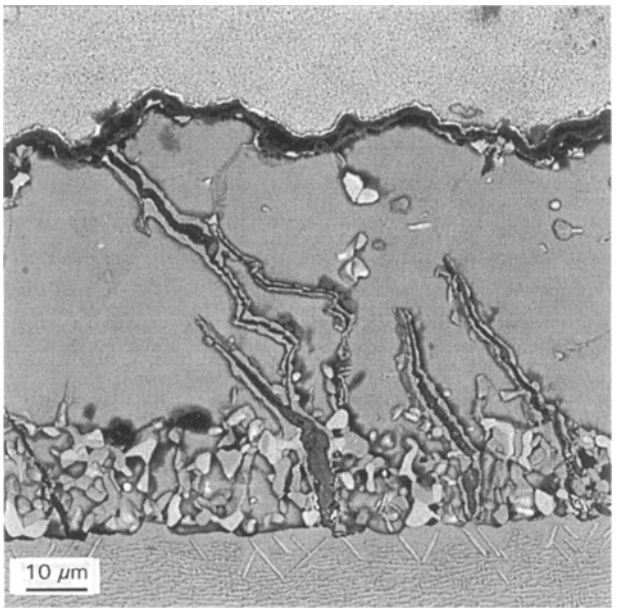

Figure 6 BSE image of cracks in sample TMF-B. Coating surface is at the top, single crystal at the bottom.

off, and become richer in chromium. The EDS/WDS analysis points to a σ-phase of composition $(Cr_{0.8}Mo_{0.2})_3(NiCo)_2$ and a phase with 80% Cr (appearing, respectively, grey and bright in Fig. 5b). The identification of the latter phase is a matter of speculation: α-Cr or a chromium carbide are often mentioned in the literature [11–14, 19]. However, in the present case the WDS carbon signal is far too low for a $M_{23}C_6$ carbide. Because of the surface contamination problem mentioned above, the quantification of carbon contents in this phase is not possible. Possible candidates for this phase are carbides or intermetallics of the form $M_{18}X$ or M_6X, also mentioned in the literature [19, 20].

The grain-boundary phase and the TiC precipitates at the main coating/coating transition layer interface

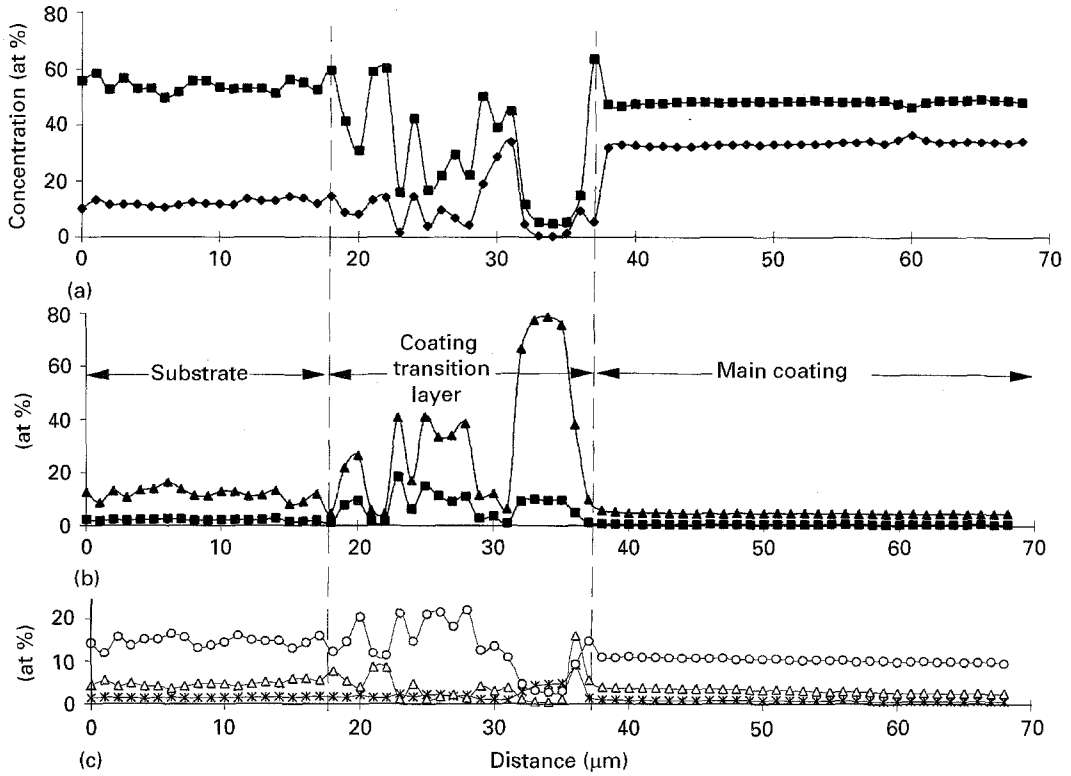

Figure 7 WDS line scans perpendicular to the coating of the TMF-B sample. (a) (◆) Al, (■) Ni; (b) (■) Mo, (▲) Cr; (c) (*) V, (△) Ti, (○) Co.

have almost disappeared. The chromium-rich particles near the surface tend to reduce in number, but those left have grown in size. EDS analysis gives a composition similar to that of the σ phase mentioned above. The composition of grain boundaries perpendicular to the surface in the main coating evolves with TMF cycling. The maps of Fig. 8 show two grain boundaries, representing two stages of this evolution. In the first stage (boundary to right of the centre of Fig. 8a), only an aluminium-depletion can be detected. When the aluminium concentration drops below the level required to stabilize the β-NiAl phase, a new phase begins to precipitate (boundary left of the centre of the figure). The EDS analysis (point 8 in Table IV) identifies it as γ′ phase, with higher titanium and aluminium contents than in the bulk. Traces of oxygen are detected in this grain-boundary phase (Fig. 8b), although no separate Al_2O_3 phase and no crack opening can be seen. The presence of oxygen can be explained by inward oxygen diffusion assisted by the stress state in the grain boundary.

In the substrate transition layer of the TMF-B sample, the round σ-phase precipitates have completely evolved to a platelet-shape, whose morphological planes are oriented with the {1 1 1} family of the single-crystal. EDS analysis of the matrix shows this phase to be γ′ with a composition identical to that in the bulk. In the bulk single crystal the interdenditric zones present an enrichment in aluminium and titanium, and a depletion in chromium, cobalt and nickel of the order of 1%. The same trend can be observed below the substrate transition layer, but with higher aluminium enrichment and nickel-depletion, owing to the diffusion processes from and to the main coating. The higher aluminium content results in a higher γ′ volume fraction (visible in Fig. 5). In this zone, an anomalous rafting of the γ′ precipitates is observed. The platelets develop almost parallel to the interface and to the stress direction already during the first testing hours (Fig. 5a), as opposed to the rafting perpendicular to the stress direction in the bulk single crystal.

3.3. LCF tested samples

Fig. 9a and b shows typical cross-sections of low-cycle fatigue-tested samples. The total high-temperature exposure times are 32.6 and 110.6 h for samples LCF-A and LCF-B, respectively. In Fig. 10 a line scan is shown for the LCF-B sample, and Table V presents the results of point analyses.

Cracks originate at the surface and stop at the interface with the substrate, or continue to grow into the substrate. At the crack tip, beyond a layer of aluminium oxide, nickel oxides form, due to the lower aluminium content in that zone.

After 32.6 h exposure at 1040 °C the substrate and coating transition layers evolved into a layer made up of the γ and the γ′ phases. In the LCF-B sample, the two phases develop into two continuous layers parallel to the substrate interface. Carbides of the type $Cr(Mo)_{23}C_6$ can be seen inside the layer and at the interface with the main coating. The strongly aluminium depleted β-NiAl phase in the main coating presents fine needle- or platelet-like precipitates. Although too small to be analysed, they show lower aluminium and higher chromium and cobalt contents than the matrix, and can be identified as σ or γ′ phase precipitates. At the interface with the oxide, both at the external surface and along cracks, massive depletion

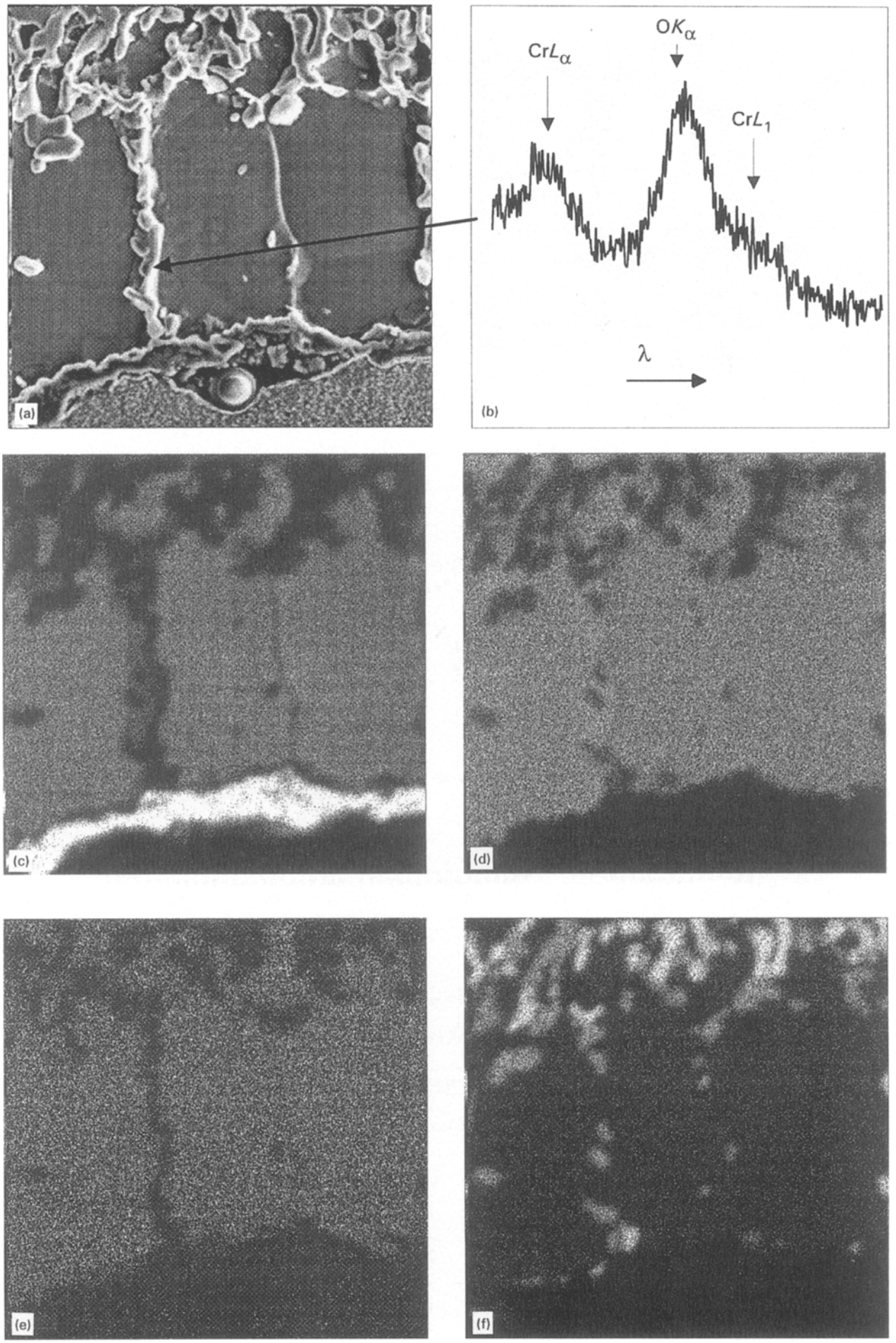

Figure 8 Grain boundaries in the TMF-B main coating: (a) secondary electrons image, (b) WDS spectrum around the oxygen K_α wavelength (2.41 nm) from the grain boundary, (c–f) elemental maps for aluminium, nickel, cobalt and chromium, respectively.

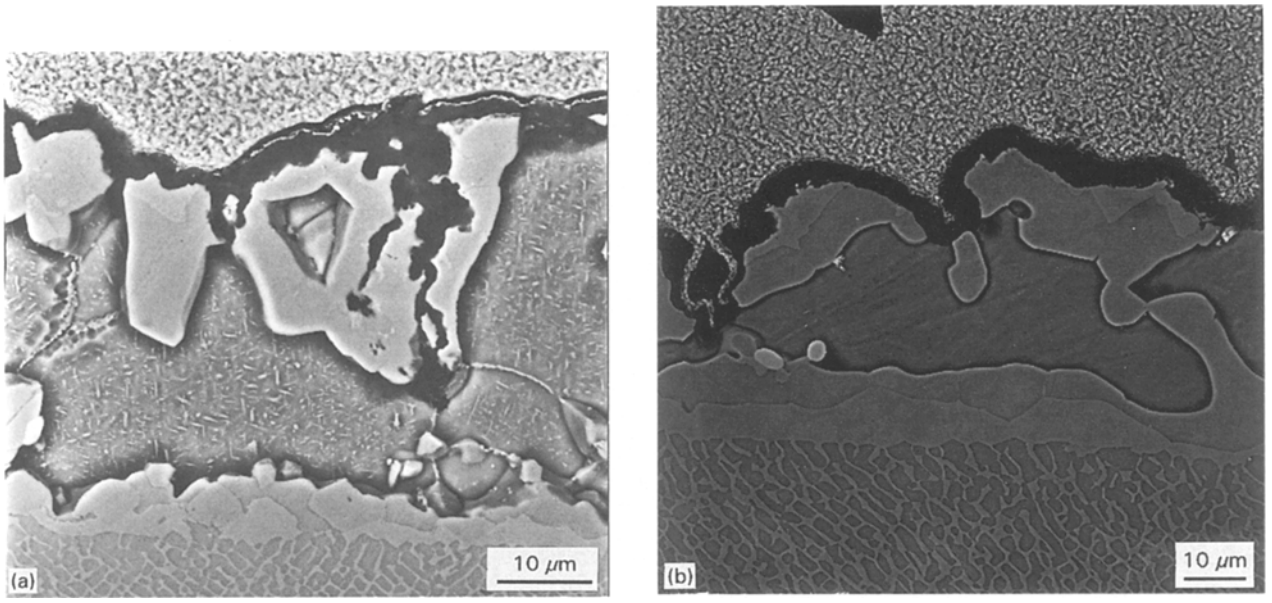

Figure 9 (a, b) BSE images of the cross-section of the low-cycle fatigued samples: (a) LCF-A, (b) LCF-B. Coating surface is at the top, single crystal at the bottom.

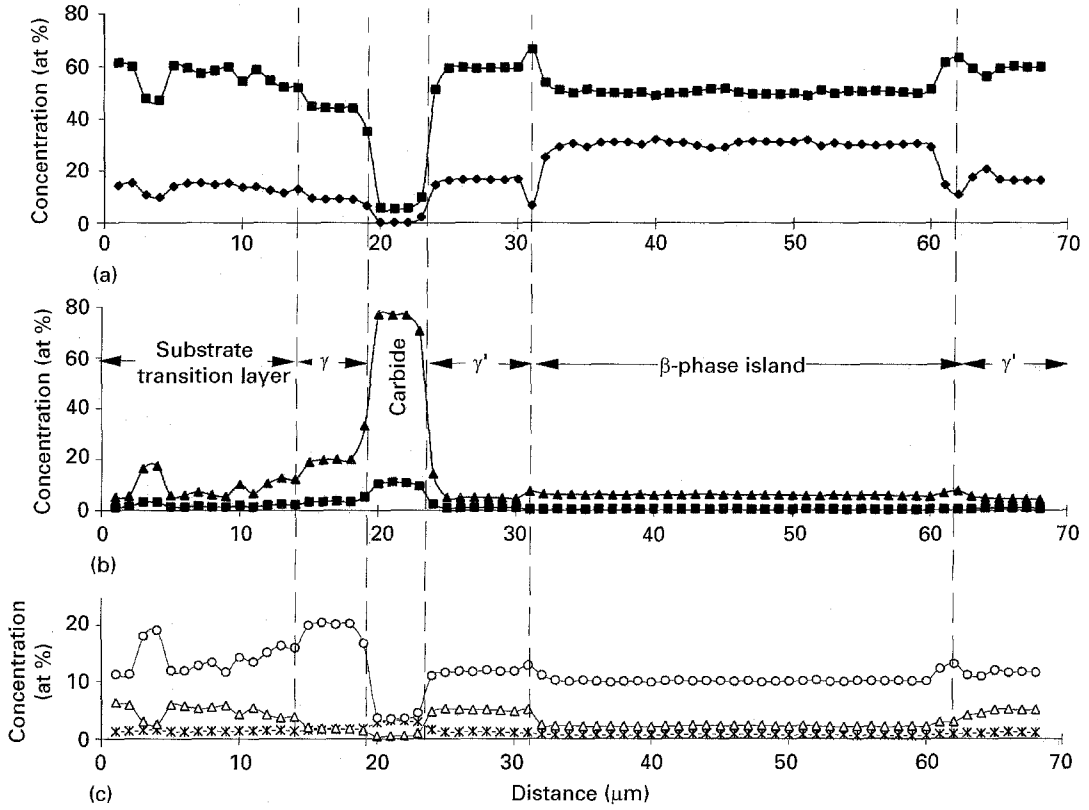

Figure 10 WDS line scans perpendicular to the coating of the LCF-B sample. (a) (◆) Al, (■) Ni; (b) (■) Mo, (▲) Cr; (c) (*) V, (△) Ti, (○) Co.

of aluminium causes the formation of γ′. While the front of the γ′ phase moves inwards into the coating, at the expense of the NiAl phase, further aluminium depletion at the oxide interface induces the nucleation of the γ phase after 110 h (LCF-B). At that time, the γ′ phase in the coating transition layer and the γ′ phase in the sub-oxide zone enter in contact and the NiAl phase re-absorbed the needle-like precipitates and reduced to islands surrounded by the γ′ phase.

4. Discussion

4.1. Chemical evolution

The microstructural evolution observed in the present study can be explained in terms of thermally activated processes [20]. Because the solubility of elements such as chromium and molybdenum is very limited in NiAl, and additionally decreases with an increase of aluminium content, chromium- and molybdenum-rich precipitates form during the coating production and

heat-treatment stages in the near-surface zone, where the aluminium content in NiAl is almost over-stoichiometric, and in the coating transition layer, where the chromium and molybdenum contents are high, owing to the proximity of the substrate. The presence of TiC precipitates can be explained in the same way. After the 16 h ageing heat treatment at 870 °C in argon (the present "as-received" condition), an intense γ' precipitation is reported in the main coating just above the coating transition layer [13], which is in line with the present observation of needle-like γ' precipitates there and in the coating transition layer. However, some inconsistency between the literature and the present results exists in the case of the as-received material. The two main precipitate phases in the coating transition layer are found to correspond to σ and γ' phases, while in the literature a highly chromium-enriched phase (α-Cr or carbides) and a σ phase are reported [13, 14]. This discrepancy cannot be explained on the basis of inaccuracies in the quantitative analysis results, related to the small dimensions of the precipitates, but can be rationalized in terms of the chemical instability of the coating transition layer. Indeed, small variations in the aluminium and chromium contents in NiAl can cause the precipitation of more or less chromium-rich secondary phases. As the analysis of the TMF-A sample demonstrates, some hours at high temperature will suffice to cause the development of richer chromium phases, due to additional chromium and molybdenum diffusion from the substrate. A subsequent prolonged exposure to the same range of temperatures (sample TMF-B) does not modify remarkably the configuration of the coating transition layer.

Under TMF conditions, the formation of an aluminium oxide layer at the surface of the coating causes the near-surface zone to deplete in aluminium, leading, as a consequence, to the dissolution of many chromium-rich precipitates. The diffusion of aluminium to the surface is so quick that already in the short lived TMF-A sample a flat aluminium profile over the main coating is observed. Because of the protective role of the oxide, the evolution of the aluminium concentration subsequent to the formation of the Al_2O_3 layer is much slower, evidence of which is given by the similar oxide scale thickness and by the constant average aluminium content in the main coating measured in the longer lived TMF-B test sample relative to the short lived TMF-A test specimen. Gale and King [13] identified an ageing mechanism as the major cause of degradation for long stress-free exposure times (above 100 h) at 850–950 °C, which resulted in the precipitation of γ' in the nickel-rich zone of the main coating and the coating transition layer. Although these γ' precipitates can be as small as 500 nm or less, accurate SEM morphological observations should enable their identification. In the present TMF samples, the presumed needle-like γ' precipitates of the as-received sample are found to dissolve in the first hours of exposure into the β matrix. This suggests that the higher temperatures encountered in the TMF cycles relative to the 850–950 °C stress-free exposure, largely speed up the general evolution of, and the damage to the coating.

In the case of the LCF-tested samples continuously exposed at 1040–1050 °C, the oxidation induced γ' formation at the surface and the interdiffusion at the coating–substrate interface, leading to the formation of continuous γ and γ' layers, are equally important degradation mechanisms. All the precipitation phases, typically occurring in the coating at lower temperatures, dissolve with time, while carbides of the form $(Cr,Mo)_{23}C_6$ develop. These microstructural observations are consistent with those of Gale and King [19] on stress-free samples exposed at 1100 °C.

4.2. Mechanical/chemical interaction

The Al_2O_3 scale observed at the TMF sample surface shows porosity, cracking and strong local differences in thickness. Moreover, the scale and the underlying coating surface show rippling or scalloping. Although no definitive conclusion can be drawn, there is some evidence that the ripple spacing correlates with the characteristic dimension of grains in the near surface zone of the main coating.

The oxide cracking is caused by the thermal mechanical cycles. In the case of steady-state conditions, the oxide forms free of stress at the exposure temperature, and can break only during cooling down. Under thermal fatigue conditions, the temperature excursion causes thermal stress to develop, with consequent scale cracking. Because of the enhanced aluminium diffusion from the grain boundary to the surface, the scale grows quicker and tends to crack easier at the grain boundary. The oxide–coating strain mismatch is additionally enhanced at grain boundaries under thermal mechanical fatigue conditions, assisting further the occurrence of repeated localized oxide breakdown. The aluminium depletion at the grain boundaries, initially due to enhanced diffusion assisted by the stress field, becomes a self-sustaining process because of the oxide cracking, which promotes additional local oxide formation. This repeated local oxidation process can also explain the rippling. Alternatively, a mechanism of kinematically irreversible cyclic creep is made responsible for the scalloping [15]. However, from both models, one would expect dramatic differences in the rippling stage between samples TMF-A and -B. On the contrary, both samples present similar ripple top-to-valley distances. This experimental evidence can probably be explained by considering that below a certain aluminium content, the β-NiAl phase becomes unstable and γ' begins to form at grain boundaries below the external oxide scale. It is conceivable that under these conditions the aluminium transport mechanism changes and slows down. Also the fact that traces of oxygen are often found at the grain boundaries in coincidence with the new phase, suggests that the local solid-state transport mechanism changes to a mainly inward diffusion type.

Oxide cracking and aluminium depletion along grain boundaries can be seen as the principal coating degradation mechanisms, which weaken the grain boundaries and create preferential sites for crack nucleation. The cracks initiate at the surface coincident with the grain boundaries, at an early stage of the

thermal fatigue cycling. Holmes and McClintock [15] identified a threshold strain of 0.14% for NiAl coating cracking on RENE N4, where he assumes that the grain boundaries open before the γ' forms. This assumption is confirmed in the case of the short-lived sample TMF-A, where the crack opening took place in the β-NiAl. In the long-lived sample TMF-B, however, the cracks developed subsequent to the γ' formation. Two experimental observations support this conclusion: γ' is frequently found at closed grain boundaries (Fig. 8), and the γ' layers show abrupt thickness variations along the crack path (Fig. 6). If the γ' phase had formed after crack opening, the layer thickness would be equal on both crack sides.

The presence of internal cracks in the TMF-B sample (Fig. 6) seems to suggest an additional degradation mechanism, which causes crack nucleation inside the coating transition layer. However, the presence of oxide and γ' layers of thickness comparable to those in external cracks can only be explained by assuming that also for these second type of cracks a direct connection to the surface exists, although not visible in the particular plane where the cross-section was performed.

Aluminium is also found to diffuse inwards, from the transition layer into the substrate. Already in the as-received sample, due to the diffusion processes which take place during coating production, the zone of the single crystal just below the substrate transition layer shows an aluminium content 1% higher relative to the composition of the dendrites in the bulk, and comparable with the bulk interdendritic composition. Aluminium diffuses further into the substrate during TMF testing, up to more than 1% above the average interdendritic composition at long exposure times. As a consequence, more γ' forms below the substrate transition layer (visible at the bottom of Fig. 5b). In this zone, an anomalous rafting of γ' precipitates into γ' platelets parallel to the interface and the stress direction is observed. This phenomenon has also been observed in other NiAl-coated nickel-base single crystals [21], and can be caused by either local variation of the chemical composition or by local anomalous stress distribution. Because of its potential importance in terms of arresting microcracks from growing into the substrate, the anomalous rafting of the γ' precipitates in the substrate transition layer deserves further research.

The coating fracture behaviour of the LCF samples is qualitatively similar to the TMF case, with nucleation of cracks at the coating surface followed by intergranular crack growth, coupled with the formation of Al_2O_3 at crack internal surfaces, and the formation of a γ' layer at the oxide-coating interface. Because both samples LCF-A and B are representative of a late stage of the coating damage evolution, it is impossible to conclude whether γ' nucleation occurs before or subsequent to crack opening.

5. Conclusions

A microstructural study of NiAl-coated nickel-base single-crystal RR2000 subjected to TMF and LCF testing has been made. The principal phases were characterized and their evolution with time and temperature investigated, in order to identify the coating degradation mechanisms and the effects of the coating on the substrate material.

1. The main morphological aspect of the coating evolution under TMF conditions is the flattening of the aluminium gradient, due to oxidation of the surface, and the re-absorption of some precipitates such as TiC and γ' phase into the β matrix. If one considers that in the range 850–950 °C these coatings should further develop γ' precipitates, as reported in the literature, it must be concluded that the fraction of the thermal cycle spent above 950 °C dominates the general fatigue behaviour. The coatings are very stable from the chemical point of view, with the surface oxidation as the major damage mechanism. Interdiffusion at the substrate–coating interface is negligible during the first hours of exposure, and only after ~100 h can an aluminium enrichment of more than 1 at % be detected in the substrate layer. After the same, long exposure times, aluminium depletion and γ' precipitation at the grain boundaries was detected in the main coating. An enhanced grain-boundary diffusion of aluminium towards the surface can be invoked as the responsible mechanism, with the subsequent formation of γ' due to aluminium depletion. The aluminium diffusion is probably assisted by repeated cracking of the protective surface oxide scale on top of the grain boundaries.

2. Fatigue cracks develop at the coating surface and grow along grain boundaries. Following cracking, the crack flanks are covered rapidly with a layer of Al_2O_3. The cracks frequently arrest inside the coating transition layer or at the interface with the substrate. While in the short-lived TMF sample, the crack opening takes place in the β-NiAl phase, evidence of cracking through the γ' phase at grain boundaries were found in the long-lived TMF sample.

3. The effect of the coating presence under TMF loading on the single-crystal is two-fold: a continuous γ' layer develops in the so-called substrate transition layer, with σ precipitates, and below it a zone of anomalous γ' rafting under TMF conditions. Both layers can strongly influence the crack growth mechanisms.

4. The major degradation mechanism of the coating during LCF loading at 1040–1050 °C is surface oxidation and interdiffusion with the substrate, which causes massive aluminium depletion and decomposition of the β phase back into γ' and γ phases. Cracks, initiating at the surface and growing intergranularly, are additional causes of oxidation and decomposition of the main coating.

Acknowledgement

The authors thank Rolls Royce plc for providing the coated specimen material.

References

1. A. STRANG and E. LANG, in "High Temperature Alloys for Gas Turbines", edited by R. Brunetaud, D. Coutsouradis, T. B. Gibbons, Y. Lindblom, D. B. Meadowcroft and R. Stickler (D. Reidel Publishing Co., Dordrecht, 1982) pp. 469–506.

2. T. E. STRANGMAN, M. FUJI and X. NGUYEN-DINH, in "Superalloys 84", edited by Gell, C. Kortovich, R. Bricknell, W. B. Kent and J. F. Radovich (The Metals Society of the American Institute of Mechanical Engineers, New York, 1984) pp. 795–804.
3. M. I. WOOD and J. E. RESTALL, in "High Temperature Alloys for Gas Turbines and other Applications", edited by W. Betz, R. Brunetaud, D. Coutsouradis, H. Fischmeister, T. B. Gibbons, I. Kvernes, Y. Lindblom, J. B. Marriott and D. B. Meadowcroft (D. Reidel, 1986) pp. 1215–26.
4. H. W. GRÜNLING, K. SCHNEIDER and L. SINGHEISER, *Mater. Sci. Eng.* **88** (1987) 177.
5. J.-M. VEYS and R. MEVREL, *ibid.* **88** (1987) 253.
6. VEYS and R. MEVREL, in "Advanced Materials and Processing Techniques for Structural Applications", edited by T. Khan and A. Lasalmonie (ONERA, Paris, 1988) pp. 168–78.
7. P. AU, R. V. DAINTY and P. C. PATNAIK, in "Surface Modification Technologies III", edited by T. S. Sudarshan and D. G. Bhat (TMS, Warrendale, PA, 1990) pp. 729–48.
8. K. R. BAIN, in "Proceedings of the *A*IAA/SAE/ASME/ASEE 21st Joint Propulsion Conference", Monterey, CA, 8–10 July 1985, American Institute for Aeronautics and Astronautics, New York, pp. 1–6.
9. H. BERNARD and L. REMY, in "Advanced Materials and processes EUROMAT '89", edited by H. Exner and V. Schumacher (DGM, Oberursel, Germany, 1989) pp. 529–34.
10. J-Y. GUEDOU and Y. HONNORAT, in "Proceedings ASTM Symposium on Thermomechanical Fatigue Behaviour of Materials", San Diego, October 1991, edited by H. Sehitoglu (ASTM STP 1186, Philadelphia, 1993) pp. 157–75.
11. P. SHEN, D. GAN and C. C. LIN, *Mater. Sci. Eng.* **78** (1986) 163.
12. *Idem, ibid.* **78** (1986) 171.
13. W. GALE and J. E. KING, *Metall. Trans.* **34A** (1992) 2657.
14. J. TOTEMEYER, W. GALE and J. E. KING, *Mater. Sci. Eng.* **A169** (1993) 16.
15. J. W. HOLMES and F. A. McCLINTOCK, *Metall. Trans.* **21A** (1990) 1209.
16. J. BRESSERS and M. BUCKLEY, to be published.
17. J. POUCHOU and F. PICHOIR, *J. Microsc. Spectrosc. Electron.* **11** (1986) 229.
18. E. NEMBACH and G. NEITE, *Progr. Mater. Sci.* **29** (1985) 177.
19. W. F. GALE and J. KING, *Mater. Sci. Technol.* **9** (1993) 793.
20. G. O. WARD and D.H. BOONE, *Oxid. Metals* **3** (1971) 475.
21. J. BRESSERS, D. J. ARRELL, K. OSTOLAZA and J. L. VALLES, "Effects of Coatings on Precipitate Rafting in Superalloys", *Mater. Sci. Eng.*, forthcoming.

Received 12 May
and accepted 1 December 1995